AGU100 ADVANCING EARTH AND SPACE SCIENCE

JGR

Journal of Geophysical Research: Solid Earth

RESEARCH ARTICLE

10.1029/2018JB016828

Key Points:
- We use differential lidar to map the slip vector distribution and shallow fault geometry for the 2010 El Mayor-Cucapah earthquake rupture
- We observe localized subsurface low-angle (<30°) oblique-normal slip
- We observe a statistical correlation between dip and slip magnitude along the low-angle structures

Supporting Information:
- Supporting Information S1

Correspondence to:
L. J. Lajoie,
llajoie@mines.edu

Citation:
Lajoie, L. J., Nissen, E., Johnson, K. L., Arrowsmith, J. R., Glennie, C. L., Hinojosa-Corona, A., & Oskin, M. (2019). Extent of low-angle normal slip in the 2010 El Mayor-Cucapah (Mexico) earthquake from differential lidar. *Journal of Geophysical Research: Solid Earth*, *124*, 943–956. https://doi.org/10.1029/2018JB016828

Received 4 OCT 2018
Accepted 16 DEC 2018
Accepted article online 21 DEC 2018
Published online 19 JAN 2019

Extent of Low-Angle Normal Slip in the 2010 El Mayor-Cucapah (Mexico) Earthquake From Differential Lidar

Lia J. Lajoie[1], Edwin Nissen[2], Kendra L. Johnson[3], J Ramón Arrowsmith[4], Craig L. Glennie[5], Alejandro Hinojosa-Corona[6], and Michael E. Oskin[7]

[1]Department of Geophysics, Colorado School of Mines, Golden, CO, USA, [2]School of Earth and Ocean Sciences, University of Victoria, Victoria, British Columbia, Canada, [3]Global Earthquake Model, Pavia, Italy, [4]School of Earth and Space Exploration, Arizona State University, Tempe, AZ, USA, [5]Department of Civil and Environmental Engineering, University of Houston, Houston, TX, USA, [6]División de Ciencias de la Tierra, Centro de Investigación Científica y de Educación Superior de Ensenada, Ensenada, Mexico, [7]Earth and Planetary Sciences, University of California, Davis,

Abstract We investigate the 4 April 2010 M_w 7.2 El Mayor-Cucapah (Mexico) earthquake using three-dimensional surface deformation computed from preevent and postevent airborne lidar topography. By profiling the E-W, N-S, and vertical displacement fields at densely sampled (~300 m) intervals along the multisegment rupture and computing fault offsets in each component, we map the slip vector along strike. Because the computed slip vectors must lie on the plane of the fault, whose local strike is known, we calculate how fault dip changes along the rupture. A principal goal is to resolve the discrepancy between field-based inferences of widespread low-angle (<30°) oblique-normal slip beneath the Sierra Cucapah, and geodetic and/or seismological models which support steeper (50°–75°) faulting in this area. Our results confirm that low-angle slip occurred along a short (~2 km) stretch of the Paso Superior fault—where the three-dimensional rupture trace is also best fit by gently inclined planes—as well as along shorter (~1 km) section of the Paso Inferior fault. We also characterize an ~8-km fault crossing the Puerta accommodation zone as dipping ~60°NE with slip of ~2 m. These results indicate that within the northern Sierra Cucapah, deep-seated rupture of steep faults (resolved by coarse geodetic models) transfers at shallower depths onto low-angle structures. We also observe a statistically significant positive correlation between fault dip and slip, with slip pronounced along steep sections of fault and inhibited along low-angle sections. This highlights the important role of local structural fabric in controlling the surface expression of large earthquakes.

1. Introduction

We investigate fault zone surface deformation and the subsurface fault geometry of the 4 April 2010 M_w 7.2 El Mayor-Cucapah earthquake in northern Baja California, Mexico (Figures 1a and 1b). This earthquake involved failure of several discrete dextral and dextral-normal faults with differing structural characteristics, making it a type example of a cascading, multifault rupture (Fletcher et al., 2014). However, in spite of an abundance of field measurements, terrestrial and airborne lidar imagery, and satellite geodetic data (e.g., Barišin et al., 2015; Fletcher et al., 2014; Gold et al., 2013; Huang et al., 2017; Oskin et al., 2012; Teran et al., 2015; Wei et al., 2011), there remain key discrepancies between models that seek to describe the underlying fault geometry. In particular, field observations in the northern rupture zone have been interpreted as indicating widespread oblique normal slip along low-angle (~20–40° dipping) normal faults underlying the Sierra Cucapah (Fletcher et al., 2014; Teran et al., 2015), whereas several independent earthquake source models based on space geodesy and/or seismology all support steeper (~50–70° dipping) faulting in this area (Fialko et al., 2010; Hauksson et al., 2011; Huang et al., 2017; Uchide et al., 2013; Wei et al., 2011; Zheng et al., 2012).

We seek to resolve this discrepancy by analyzing fault zone deformation in the El Mayor-Cucapah earthquake mapped from preearthquake and postearthquake airborne lidar topography (Glennie et al., 2014). These near-field geodetic data help bridge a gap between offsets surveyed in the field and those determined over larger apertures from satellite imagery and—in revealing fault zone displacements in three dimensions—provide an unusual opportunity to test for the involvement of low-angle detachment faulting.

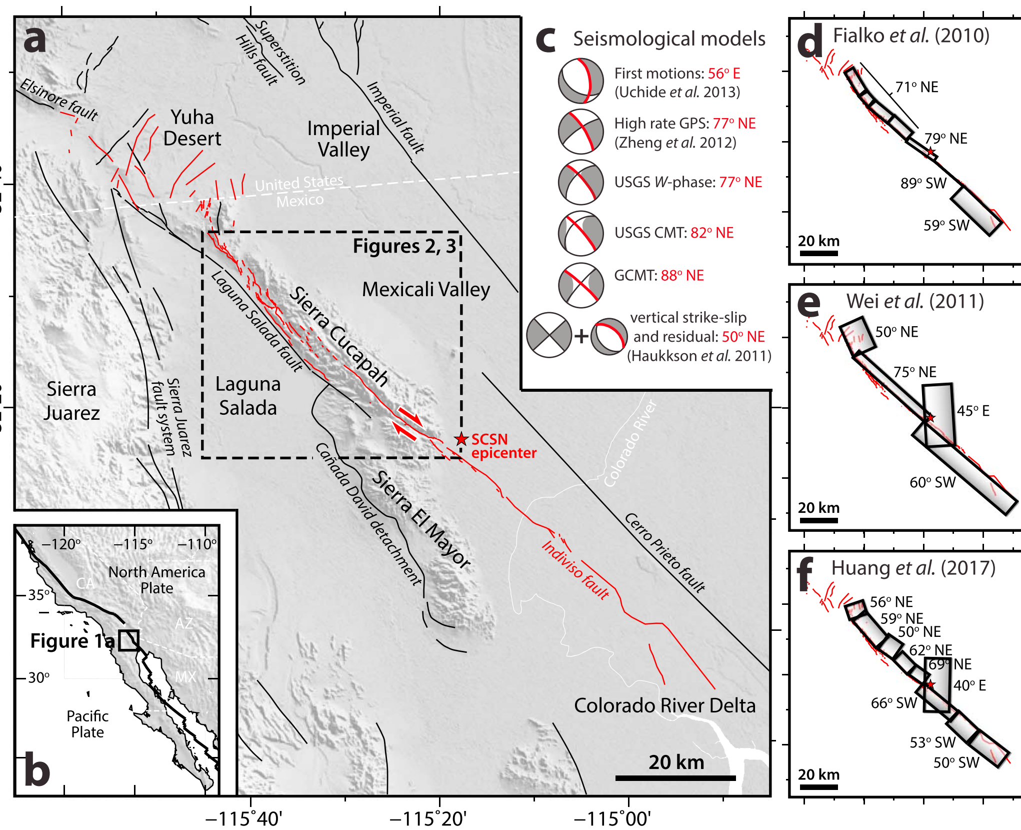

Figure 1. (a) Tectonic setting of the 4 April 2010 El Mayor-Cucapah earthquake. The red star is the epicenter from the Southern California Seismic Network (SCSN), red lines show the principal surface ruptures from Fletcher et al. (2014), and black lines show other active faults. (b) Inset showing wider tectonic setting with the main Pacific-North America plate boundary in bold. (c) Focal mechanisms from seismology with red numbers indicating the dips of the E or NE-dipping nodal planes, marked in red. (d–f) Finite fault models derived from Interferometric Synthetic Aperture Radar and pixel correlation measurements, from Fialko et al. (2010), Wei et al. (2011), and Huang et al. (2017). Map extents are the same as in (a) and the red star is the SCSN epicenter. Each gray rectangle is an individual model fault segment, shaded darker down dip and labeled with its dip and dip direction.

This is an important issue for a variety of reasons. First, normal slip along gently dipping fault planes is mechanically unfavorable (e.g., Anderson, 1905, 1951) and resolving the extent of it in the El Mayor-Cucapah earthquake is thus important for the long-standing debate over whether low-angle normal faults host large earthquakes (e.g., Abers, 1991; Axen, 1999; Jackson & White, 1989; Proffett, 1977; Styron & Hetland, 2014; Wernicke, 1995) and whether multifault ruptures provide a mechanism by which they can do so (Fletcher et al., 2016). Second, there are regional implications for how oblique extension is accommodated along this section of the Pacific-North America plate boundary (Axen et al., 1999; Fletcher & Spelz, 2009; Mueller et al., 2009; Nagy et al., 2000). Finally, the mechanism of the El Mayor-Cucapah earthquake has an important bearing on stresses transferred to neighboring faults, and thus regional seismic hazard. For instance, widespread oblique slip along a shallow-angle, NE dipping detachment could lead to a significant reduction of normal stresses on the Imperial and Superstition Hills faults to the NE (Figure 1a). Previous studies of triggered slip or seismicity rate changes on neighboring faults following the El Mayor-Cucapah earthquake may have estimated Coulomb stresses using model fault geometries that may be inaccurate in light of our work (Meng & Peng, 2014; Wei et al., 2015). Though a full slip model for this earthquake—and an ensuing Coulomb stress change calculation—lie beyond the scope of this study, we hope that our new constraints on the shallow fault geometry will inform future efforts on this topic.

2. Overview of the El Mayor-Cucapah Earthquake

The M_w 7.2 El Mayor-Cucapah earthquake struck northern Baja California, Mexico (Figure 1a) at 22:40 UTC on 4 April 2010, causing major damage to Mexicali and Calexico where four people were killed and more than 100 injured. The epicenter was situated at the intersection of the Sierra El Mayor and Sierra Cucapah mountain

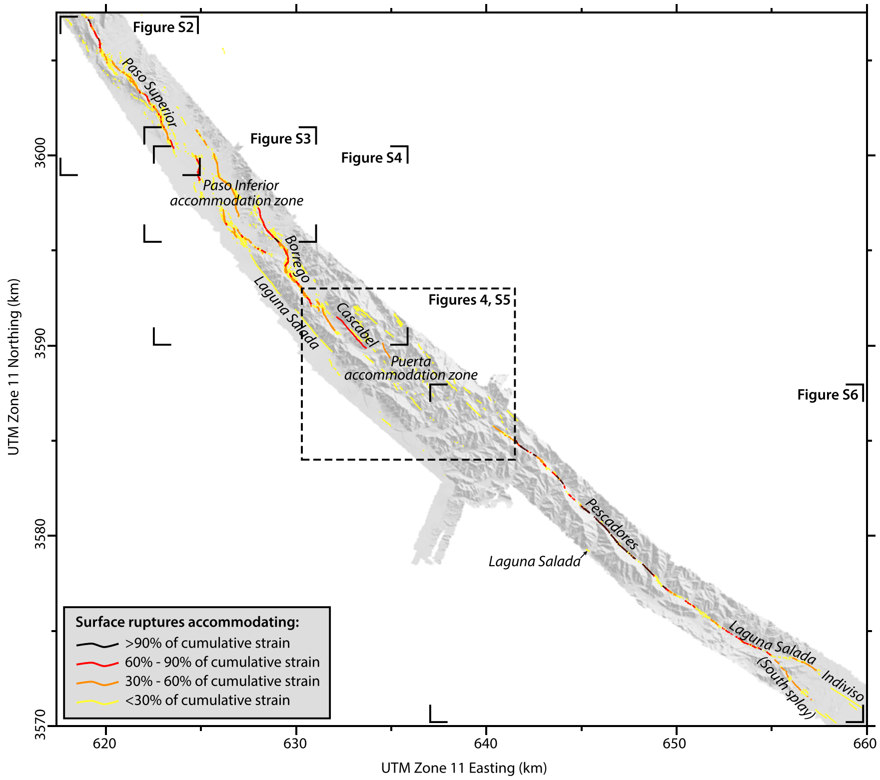

Figure 2. Rupture trace within the Sierra Cucapah mountains, colored according to the proportion of the cumulative fault zone slip each segment locally accommodates, using data from Teran et al. (2015). Background hillshaded topography shows the postevent lidar data set.

ranges, subparallel uplifts composed of Mesozoic igneous and metamorphic rocks and Tertiary volcanics and sediments which separate the Mexicali Valley to the northeast from the Laguna Salada basin to the southwest (Fletcher et al., 2014). Aftershocks form a ~120-km-long, ~10-km-wide band that extends northwest of the epicenter along the axis of the Sierra Cucapah range to just north of the U. S. border, and southeast of the epicenter across the Colorado river delta (Castro et al., 2011; Hauksson et al., 2011).

Coseismic surface faulting was initially mapped using Interferometric Synthetic Aperture Radar (InSAR) and satellite pixel offsets (Fialko et al., 2010; Wei et al., 2011), later enhanced by more detailed lidar and field-based measurements (Fletcher et al., 2014; Oskin et al., 2012; Teran et al., 2015). This revealed faulting extending along the full length of the main aftershock zone and encompassing several discrete fault segments. Southeast of the epicenter, the earthquake ruptured the previously unrecognized Indiviso fault within thick (up to ~5 km), actively subsiding deltaic deposits of the Colorado River (Figure 1a). Northwest of the epicenter, the earthquake ruptured a left stepping, en echelon array of N to NW striking faults within the Sierra Cucapah—the Laguna Salada, Pescadores, Borrego, and Paso Superior faults—before terminating at the U.S. border (Figure 2).

A surprising aspect of the earthquake is that it ruptured into stress shadows of recent events on adjacent, subparallel faults (Fialko et al., 2010; Fletcher et al., 2014). The surface traces of the Paso Superior and Borrego faults lie within 1–2 km of the western Sierra Cucapah range front, where the W dipping Laguna Salada fault ruptured in a $M \sim 7$ earthquake in 1892 (Hough & Elliot, 2004; Mueller & Rockwell, 1995; Rockwell et al., 2015). The Indiviso fault lies ~10 km southwest of the Cerro Prieto fault which hosted $M_w \sim 7$, 6.1, and 5.4 earthquakes in 1934, 1980, and 2006, respectively (Suárez-Vidal et al., 2007). Faulting in this region collectively accommodates ~4–5 cm/year of NW-SE right-lateral shear at this latitude (González-Ortega et al., 2018), but how this strain rate is distributed among individual structures is currently poorly understood.

2.1. Seismological Rupture Models

Focal mechanisms derived from seismology characterize the aggregate sense of slip in the earthquake but also provide an indication of the complexity of faulting involved (Figure 1c). A double-couple solution calculated from P wave first motions, and therefore representative only of initial faulting at the earthquake hypocenter, indicates oblique slip along moderately E dipping (normal/left-lateral) or SW dipping (normal/right-lateral) planes (Uchide et al., 2013). A double-couple mechanism derived from modeling surface waves recorded by high-rate GPS stations in southern California supports almost pure right-lateral strike slip along a 77°NE dipping fault (Zheng et al., 2012). Mechanisms determined from regional and teleseismic surface waves by the USGS National Earthquake Information Center and Global Centroid Moment Tensor project have similar nodal planes but contain a large nondouble-couple component, implying source complexity. Hauksson et al. (2011) deconvolved the Global Centroid Moment Tensor solution to show that the non-double couple component is consistent with vertical NW–SE trending strike-slip faulting and additional, parallel normal faulting.

Most aftershock mechanisms mimic the mainshock moment tensor solutions, though a cluster of events close to the mainshock epicenter involve normal faulting on moderate-angle NE or SW dipping planes (Hauksson et al., 2011). Most of those that were well-recorded locally have hypocenters shallower than 15 km, with a few at greater depths of up to ~30 km (Castro et al., 2011). Several thousand aftershocks at the northern end of the rupture, detected and relocated using a temporary seismic deployment in southernmost California, align closely with a series of short, conjugate (NE and NW trending) ruptures mapped in the Yuha desert (Fletcher et al., 2014; Kroll et al., 2013; Ross et al., 2017; Rymer et al., 2011).

2.2. Satellite Geodetic Rupture Models

Elastic dislocation modeling of Interferometric Synthetic Aperture Radar (InSAR) line-of-sight displacements, horizontal satellite pixel offsets, and regional GPS velocities have provided more detailed constraints on the subsurface fault geometry that are independent from the seismological solutions. To date, there are four published coseismic fault slip models based on subsets of these data (Fialko et al., 2010; Huang et al., 2017; Wei et al., 2011; Xu et al., 2016). Though the detailed model fault geometries and slip distributions differ, they are all in agreement on three key aspects of the earthquake: (1) that faulting in the main NW-SE rupture zone is steeply dipping (~50–90°), consistent with the seismological moment tensor solutions, (2) that coseismic faulting penetrates to depths of 10–15 km, consistent with the base of the main aftershock zone, and (3) that the greatest slip occurs at depths of 3–6 km such that there is a clear shallow slip deficit. However, we also note that each of these models approximates the en echelon rupture pattern in the northern Sierra Cucapah (described in more detail in section 2.3) as a continuous, near-linear trace. These models might be biased toward steeper dip angles in an effort to fit a single plane across the en echelon segments. The InSAR imagery also contains data gaps along the entire surface rupture, where steep phase gradients and/or heavy ground shaking are likely to have caused decorrelation.

An initial elastic dislocation model by Fialko et al. (2010) indicates 59° and 89°SW dips along the southern and northern Indiviso fault, a 79°NE dip on the Laguna Salada fault, and 71°NE dips on three segments that approximate the Pescadores, Borrego, and Paso Superior faults (Figure 1d). This model has since been used as the basis for dynamic rupture simulations (Kyriakopoulos et al., 2017) and modeling of postseismic deformation (González-Ortega et al., 2014). An alternative model by Wei et al. (2011) shows a 60°SW dip on the Indiviso fault, a 60°NE dip for a fault segment approximating the Laguna Salada, Pescadores, and Borrego faults, and a 50°NE dip for the Paso Superior fault (Figure 1e). They also invoke slip along a 45°E dipping normal fault at the southern end of the Sierra Cucapah, which corresponds to the earthquake hypocenter and accounts for its first motion mechanism. A third slip model, by Xu et al. (2016), involves six steeply dipping fault segments in a similar arrangement to the Fialko et al. (2010) model, but the exact parameters are not reported and so we do not show the model in Figure 1. A fourth, nine-segment slip model by Huang et al. (2017) indicates dips of 50–66°SW on the Indiviso fault, 62–69°NE on the Laguna Salada, Pescadores, and Borrego faults, 50° and 59°NE on two segments of the Paso Superior fault (Figure 1e). This model also includes a fault at the earthquake epicenter itself, which dips 40°E.

Kinematic rupture models, which take the fault geometries derived from geodesy and map the progression of slip from seismological data, reveal important additional properties of the earthquake (Uchide et al., 2013; Wei et al., 2011). Slip initiated along an E dipping normal segment before progressing bilaterally onto the Indiviso and Laguna Salada faults after 15–20 s. Strong high-frequency radiation ~50 km northwest of the hypocenter after ~28 s may correspond to the step-over between the Borrego and Paso Superior faults. Finally, rupture ceases simultaneously at the northwestern end of the Paso Superior fault and the southeastern end of the Indiviso fault after ~50 s.

10.1029/2018JB016828

2.3. Field Observations of Surface Faulting

The El Mayor–Cucapah earthquake generated ~120 km of surface ruptures from the Colorado River delta in the SE to the US-Mexico border in the NW. Initial rupture mapping was facilitated by lidar surveys undertaken both before and after the earthquake and by vertical differencing of these data (Oskin et al., 2012). Subsequently, extensive field measurements have detailed variations in surface slip, slip sense, and fault dip along the primary rupture trace (Fletcher et al., 2014), as well as changes in the width, thickness, and internal strain distribution of a broader fault damage zone (Teran et al., 2015). These studies also describe the structural and geomorphological context of the surface ruptures.

Close to the epicenter, liquefaction features reported by Fletcher et al. (2014) may relate to the E dipping normal fault that hosted initial slip in the earthquake (Uchide et al., 2013; Wei et al., 2011). Fletcher et al. (2016) pointed out that within the regional stress field this fault is unfavorably oriented for slip; it may have acted as a "keystone" that held more favorably oriented, neighboring faults in place, before eventually failing and causing the entire network of faults to break. Southeast of the epicenter, the newly identified Indiviso fault produced a distributed zone of en echelon fractures and liquefaction within thick deltaic deposits of the Colorado River, but local slip magnitude and rupture geometry are difficult to determine due to the lack of a discrete, laterally continuous surface trace (Fletcher et al., 2014). The epicentral and Indiviso faults lie outside the area of coherent differential lidar displacements determined by Glennie et al. (2014), and so we do not discuss them further in this study.

Northwest of the epicenter, the surface rupture crosses the Sierra Cucapah (Figure 1a), a ~50-km-long mountain range composed of Mesozoic igneous and metamorphic rocks and Tertiary volcanics and sediments (Barnard, 1969; Fletcher et al., 2014). Here it ruptured across a left-stepping, en echelon array of mostly NE dipping faults, as well as two broad accommodation zones containing more distributed deformation, interpreted as structural relays between these faults (Figure 2). From southeast to northwest (and hence in the local rupture propagation direction), the main rupture segments comprise the subvertical Laguna Salada fault, the ~70° NE dipping Pescadores fault, the ~40° NE dipping Borrego fault, and the ~20° NE dipping Paso Superior fault. The progressive reduction in dip suggested that these faults form an imbricate stack or fan, with the structurally lowest of them—the Paso Superior fault—the master fault onto which the others sole into at depth (Fletcher et al., 2014). The Paso Superior fault is a major geological contact juxtaposing Neogene sediments with Mesozoic crystalline basement and appears to be the most structurally mature of the faults that ruptured in the El Mayor-Cucapah earthquake, based on well-developed gouge, breccia, chloritic alteration, and cataclasite.

Field measurements of surface slip within the Sierra Cucapah average ~2 m but locally reach 3–4 m on all four main faults (Fletcher et al., 2014). The slip sense varies locally from pure dextral, through normal-dextral, to pure normal, with the strike- and dip-slip components sometimes partitioned between neighboring strands. In general, the steeper, southern faults have larger dextral and smaller normal components than the more gently inclined, northern faults. The rupture zone fabric also varies widely, with the broadest damage zones generally associated with the shallowest-dipping Borrego and Paso Superior fault segments (Teran et al., 2015). At one locality, the latter fault hosted >3 m of oblique surface slip along a plane inclined at just ~20°, and so a primary interest of ours is determining the extent of low-angle slip on this important regional structure.

The ~10-km-wide Puerta accommodation zone links the Pescadores and Borrego faults (Figure 2). Though only a few scattered ruptures were identified on the ground and surface faulting is hard to discern from lidar elevation changes, satellite pixel tracking indicates a sharp, near-continuous horizontal displacement discontinuity crossing the Puerta accommodation zone (Fletcher et al., 2014; Wei et al., 2011). It is possible either that the surface trace of the rupture is largely obliterated by coseismic mass wasting, or that slip at depth failed to propagate upward all the way to the surface. The ~5-km-wide Paso Inferior accommodation zone, which links the Borrego and Paso Superior faults, contains several short NE dipping fault scarps and one longer one that dips toward the SW. Lidar elevation changes appear to show kilometer-scale bending across the Paso Inferior accommodation zone, perhaps accounting for the extensive ground cracking that was observed even away from these scarps. The rupture terminated in a third zone of distributed deformation just north of the US-Mexico border (Rymer et al., 2011), but these short, scattered fault segments lie outside the bounds of Glennie et al.'s (2014) displacement data set and so are not a focus of this study.

10.1029/2018JB016828

3. Data and Methods

3.1. Three-Dimensional Surface Displacement Field From Differential Lidar

We analyzed the El Mayor-Cucapah rupture geometry using the 100-m-resolution surface deformation data set of Glennie et al. (2014), which was calculated by aligning 100-m windows of preevent and postevent lidar point clouds using the Iterative Closest Point (ICP) algorithm (Nissen et al., 2012, 2014). The preevent lidar data belong to a regional survey by the Instituto Nacional de Estadistica y Geografia flown in August 2006 and have an average density of ~0.013 points/m^2. The postevent data were collected by the National Center for Airborne Laser Mapping in August 2010, 4 months after the earthquake. They are higher density than the preevent data, averaging ~10 points/m^2, but cover a relatively narrow (~3- to 5-km-wide) swath centered on the surface rupture. This pair of data sets were first analyzed by Oskin et al. (2012), who mapped coseismic elevation changes by subtracting preevent from postevent gridded digital terrain models. However, this strategy does not account for lateral displacements and so cannot directly resolve surface *displacements*. Elevation changes are also of limited value in parts of the rupture zone characterized by rugged topography and where horizontal motions exceed vertical ones.

In contrast, by aligning windowed lidar point clouds using ICP, Glennie et al. (2014) captured the surface displacement vectors in three dimensions, as well as three rotation components. Barišin et al. (2015) produced a similar data set by correlating in two dimensions preevent satellite photographs with the postevent lidar, correcting digital elevation models for these horizontal shifts and subtracting for the vertical component, but the resulting displacement fields are noticeably noisier than those of Glennie et al. (2014) and so we choose to work with the latter. Figures 3a–3c show the resulting *x* axis (E-W), *y* axis (N-S), and *z* axis (up-down) displacements, and Figure 3d shows the *y* axis rotations. In Figure 3d, pixels containing large eastward (positive) or westward (negative) tilts, respectively, illuminate the various E and W dipping fault scarps, but we do not otherwise utilize the cell rotations, focusing here on the displacement fields. These exhibit coherent deformation throughout much of the coverage area, but there are nevertheless some important limitations. First, Glennie et al. (2014) found that there was insufficient relief within the Colorado River delta and Laguna Salada basin to resolve coherent horizontal displacements in these areas. Second, initial results were hampered by large N-S trending artifacts related to errors in the preevent survey data. Reprocessing of the preevent lidar has reduced but not entirely eliminated these artifacts from the displacement fields (Glennie et al., 2014), and we find that they are particularly problematic within the Puerta accommodation zone.

3.2. Estimating Fault Dip From the 3-D Surface Displacement Field

To analyze the subsurface geometry of the El Mayor-Cucapah faults, we first mapped offsets in each component of the displacement field at regular intervals along the length of the surface rupture. The *x*, *y*, and *z* offset at any point on a fault represents the local Cartesian slip vector, which must lie in the plane of the fault, so we can then use knowledge of the local fault strike to compute the fault dip. Geometrically, this is done by projecting the slip vector onto a vertical plane orthogonal to the local fault strike and calculating its inclination. We also measure rake by taking the dot product of the strike and slip vectors. An important limitation to this method arises along faults with horizontal slip vectors that parallel the fault strike—in other words, where the rake is purely strike slip. In this instance, *any* plane with the fault strike contains the slip vector, making fault dip impossible to resolve. We discuss this limitation as it applies to the oblique normal-dextral El Mayor-Cucapah rupture in section 4.

To determine robust slip vectors, we developed and applied a semi-automated procedure for extracting offsets from fault trace-perpendicular swath profiles through the *x*, *y* and *z* surface displacement fields. The swath profiles are centered at 300 m intervals along Fletcher et al.'s (2014) digitized fault surface trace (exact centerpoint locations are shown in Supplementary Figures S2–S6) and extend orthogonally on either side of the fault to the edge of the lidar double coverage. After testing, we found that a swath width of 300 m is the narrowest that still provides a sufficient number of data points to ensure a robust result. All points within the swath were projected onto the central profile line. Offsets were measured separately in each of the *x*, *y*, and *z* displacement fields using straight-line, least squares fits through the data points on each side of the fault, projecting to the fault, and computing the line separation at the fault (Milliner et al., 2015). We similarly calculated, projected, and differenced 1σ uncertainties, in order to determine the error in each slip vector measurement. In our implementation, the user can define for each profile the limits for curve fitting on either side of the fault, allowing for some human discretion in avoiding artifacts and accounting for the variable width (tens to hundreds of meters) of the near-fault damage zone. We were particularly careful analyzing profiles that straddled or partially straddled the N-S trending displacement artifacts, so as to avoid including the artifact in the

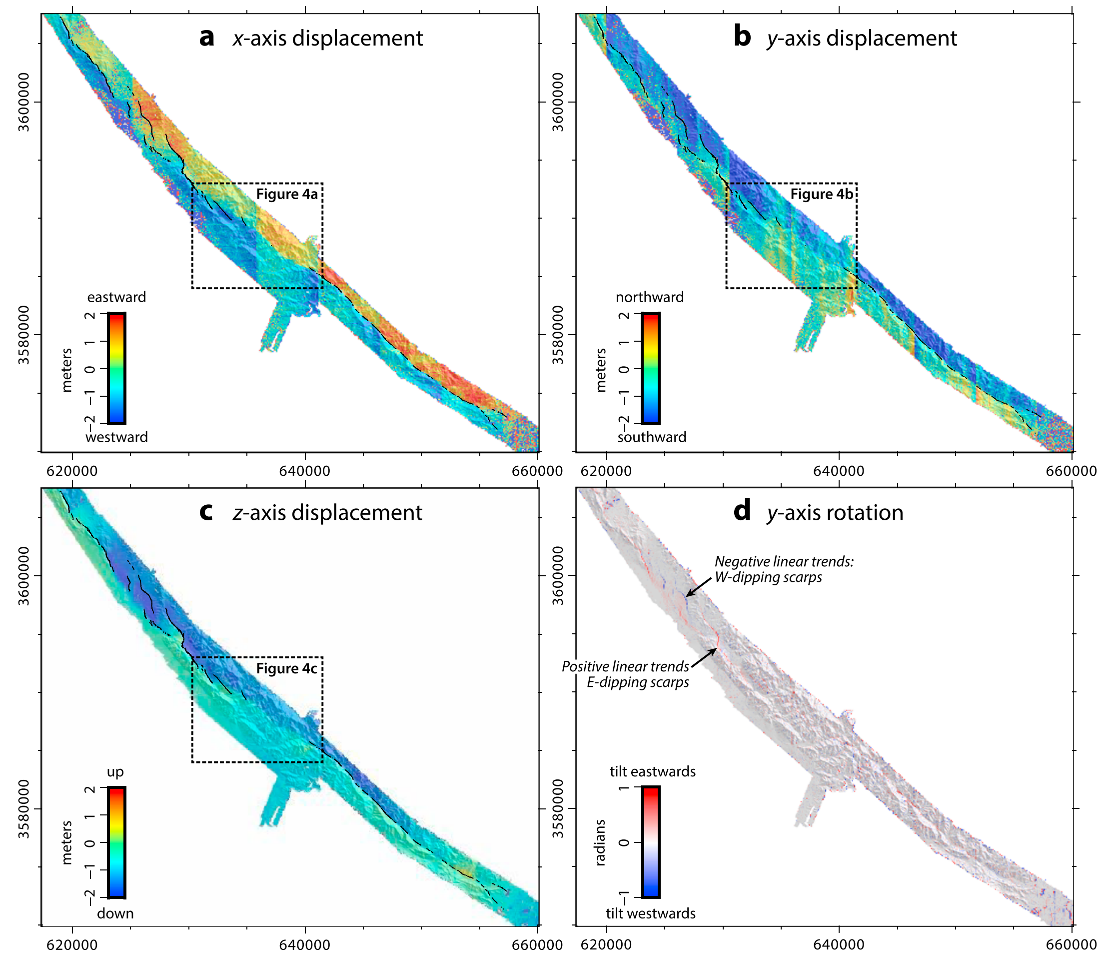

Figure 3. Iterative Closest Point results for a cell size of 100 m, with map extents as in Figure 2 and UTM zone 11 coordinates. Panels (a) to (c) show translation components in the *x*, *y*, and *z* axis directions, with positive values indicating motion toward the E, N, and upward, respectively. Major ruptures, locally accommodating >30% of the cumulative fault zone slip, are indicated by black lines (Teran et al., 2015). Panel (d) shows rotations about the *y* axis, with positive values indicating clockwise rotations about the positive axis direction (i.e., tilt toward the east). The annotated faults are the longest, W dipping strand of the Paso Inferior accommodation zone (in the north) and the E dipping Borrego fault (in the south). For ICP *x* and *z* axis rotations, see Figure S1 in the supporting information.

measured offset. By using linear displacement trends recorded hundreds of meters from the fault, we avoided complications from off-fault damage zone deformation or free surface effects, and so we consider that the resulting measurements sample faulting at depths of tens to hundreds of meters (Nissen et al., 2014; Scott et al., 2018).

In this way, we analyzed the four main Sierra Cucapah faults identified by Fletcher et al. (2014): the Paso Superior fault, which we divided into two segments, the Borrego fault, and the Pescadores and Laguna Salada faults, which we treated as one continuous structure. In addition, we studied the longest of the faults within the Paso Inferior accommodation zone as well as a sixth fault crossing the Puerta accomodation zone to link the Borrego and Pescadores faults. The Puerta accommodation zone contains no continuous mapped surface rupture, but—consistent with the pixel tracking results of Wei et al. (2011) and Barišin et al. (2015)—there is a clear discontinuity in the *x*, *y*, and *z* displacement fields, which is kinked or undulating in map view but which we approximated as a single, linear trace (Figures 4a–4c).

3.3. Estimating Fault Dip From the 3-D Surface Rupture Trace

For an independent check on the dip along the reported lowest-dip angle rupture section—the Paso Superior fault—we adopted a method for computing fault dip using only the high-resolution postearthquake lidar topography (Zhou et al., 2016). By fitting planes through the 3-D rupture trace, which is the intersection of the underlying fault plane with topography, we can estimate the fault dip representative of the shallow depths

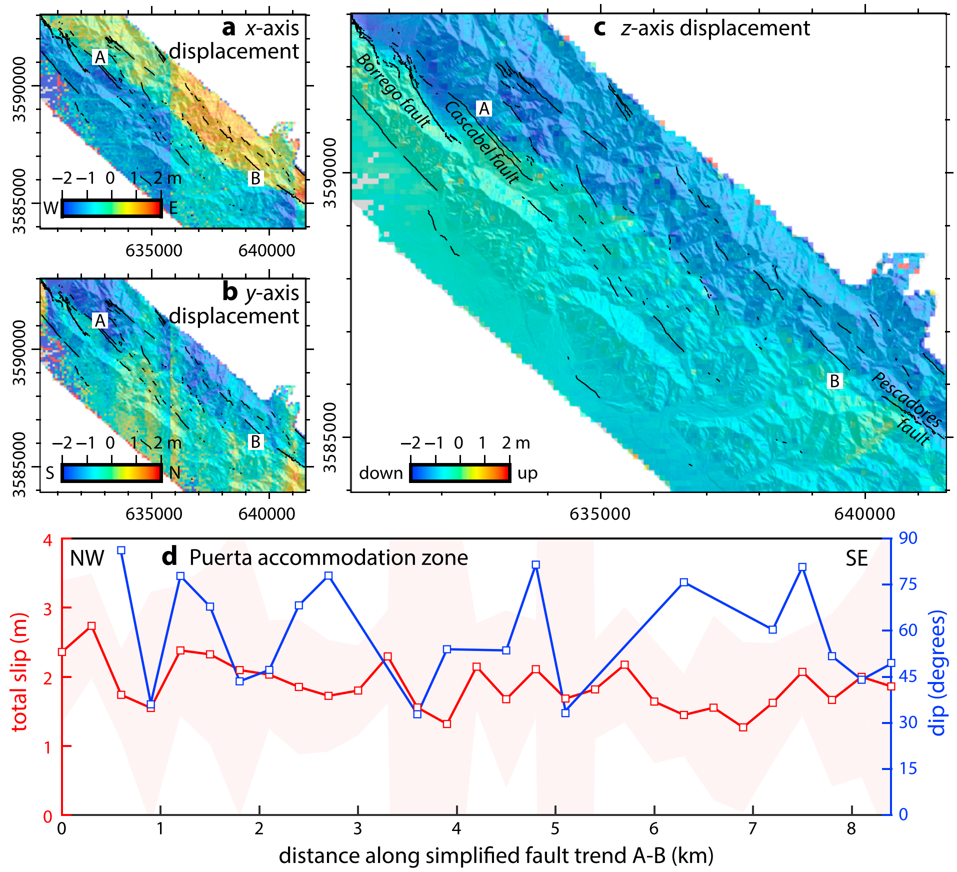

Figure 4. (a–c) Iterative Closest Point x, y, and z axis displacements within the Puerta accomodation zone. Points A and B are the endpoints of the profile in (d). Faults are marked by black lines, with those accommodating >30% of cumulative strain labeled in (c) (Teran et al., 2015). (d) Along-strike profiles of fault dip (small blue/white squares mark individual displacement swath centerpoints, connect by the blue line) and slip (small red/white squares, connected by the red line, with 1σ uncertainties in pink) between points A and B in the Puerta accommodation zone. Because of the strong right-lateral slip component and the oversimplified fault surface trace, we consider only the *average* results for this fault—a fault dip of ~60° NE and slip of ~2 m—as robust. The centerpoints of individual displacement swath profiles are plotted in map view in Figure S5 in the supporting information.

(tns to hundreds of meters) sampled by the local relief. We estimated the fault dip separately for four segments of the Paso Superior fault and avoided estimating it across the segment boundaries where plane fitting is unlikely to produce meaningful results. We digitized simplified surface traces of the four segments, guided jointly by Fletcher et al., 2014's (2014) principal rupture trace and the ICP surface displacement fields (whose major discontinuity generally lies a short distance to the southwest). Each digitized rupture trace comprised roughly ~100 vertices at ~5-m point spacing. Following Zhou et al. (2016), we computed the dip, θ, of each segment by minimizing least squares residual distances d_i between the fault trace vertices, x_i, y_i, and z_i, and a plane defined by the plane equation coefficients, A, B, C, and D (equations (1)–(3)):

$$A \cdot x + B \cdot y + C \cdot z + D = 0 \tag{1}$$

$$d_i = \frac{|A \cdot x_i + B \cdot y_i + C \cdot z_i + D|}{\sqrt{A^2 + B^2 + C^2}} \tag{2}$$

$$\theta = \frac{\pi}{2} - \tan^{-1} \frac{C}{\sqrt{A^2 + B^2}} \tag{3}$$

To ensure robust segment dip values, we additionally performed a bootstrapping statistical analysis to minimize the impact of erroneous points incorrectly identified as lying upon the primary surface rupture. In each

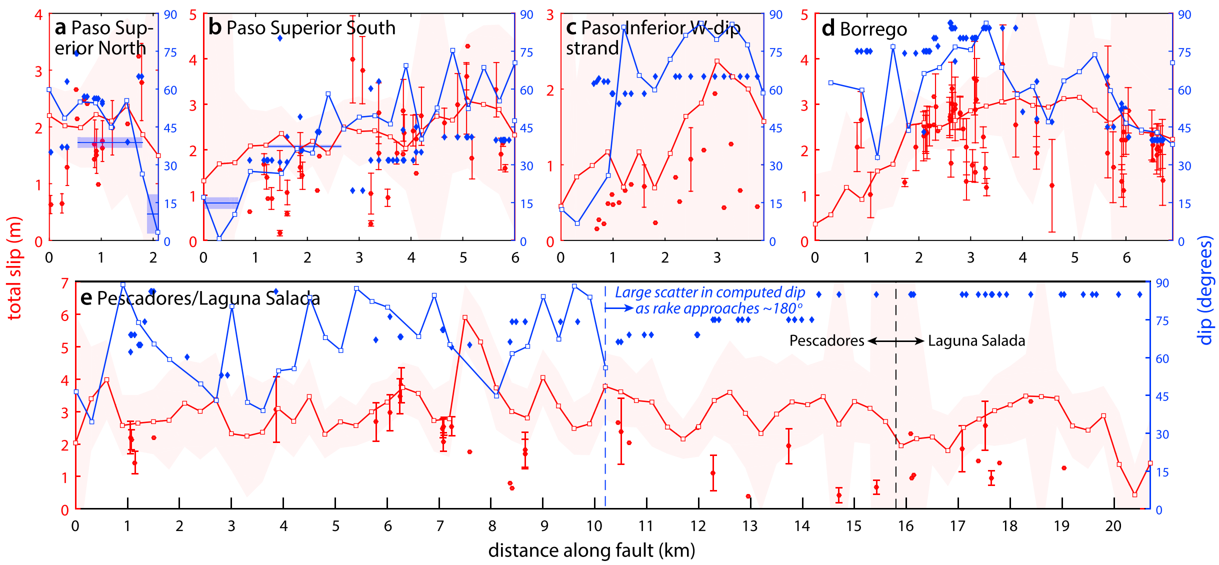

Figure 5. Along-strike profiles of fault dip (small blue/white squares mark individual displacement swath center points, connect by blue lines) and slip (red/white squares, connected by red lines, with 1σ uncertainties in pink) for (a, b) the Paso Superior fault, (c) the longest, W dipping strand of the Paso Inferior accommodation zone, (d) the Borrego fault, and (e) the Pescadores and Laguna Salada faults. The NW end of each fault is at 0-km distance on the *x* axis. Corresponding field measurements of dip (blue diamonds) and slip (red circles) are from Fletcher et al. (2014). In (a) and (b), horizontal blue lines show auxiliary dip estimates from plane fitting through four short sections of the Paso Superior fault trace, with blue boxes indicating standard errors. In (e), the short section of dip measurements toward the SW is marked dashed. The center points of individual displacement swath profiles are plotted in map view in Figures S2–S4 and S6.

iteration, we found the planar fit to a randomly selected 70% of the scarp points, repeating this test 1,000 times to yield a distribution of planar fits from which uncertainties were calculated.

4. Results

Along-fault slip and dip profiles are shown in Figure 4d (Puerta accommodation zone) and Figure 5 (other faults). An important general observation is that where the rake approaches 180° (pure right lateral), our computed dip values are highly variable. This reflects the fact that where the slip vector is both subhorizontal and subparallel to local fault strike, small errors in measured *x* and *y* offsets translate into large errors in dip (section 3.2). Consequently, we have filtered from our results all dip measurements for which our computed rake is less than 20° from pure right lateral; this includes the entire southern half of the Pescadores-Laguna Salada section (Figure 5e). Below, we discuss our detailed results in geographical order, starting at the northern end of the rupture (and, thus, in reverse order of rupture propagation).

The Paso Superior fault is of particular interest as it encompasses some of the key field localities in which low-angle slip was observed on the ground (Fletcher et al., 2014; Teran et al., 2015). Figures 5a and 5b show our displacement field-derived estimates of fault dip (blue line) and slip vector magnitude (red line, with pink shading indicating 1σ error); our independent scarp trace-derived estimates for fault dip (four horizontal blue lines, with blue shading for 1σ errors); and, for comparison, field measurements of fault dip (blue circles) and total slip (red circles with vertical error bars) from Fletcher et al. (2014). These are plotted as a function of distance along the curved fault traces. Our dip estimates are mostly consistent with the lower end of the field measurements and exhibit significantly less short-wavelength scatter; our slip measurements also vary more smoothly along strike than those of the field survey, though generally agree within error. This likely reflects that the fault geometry and slip exposed at the primary rupture trace are often influenced by surficial effects, including off fault deformation, shallow branching, refraction (steepening) of the fault toward the Earth free surface, and the tendency for unconsolidated surficial materials to fail in tension (Fletcher et al., 2014; Teran et al., 2015). The lidar measurements, in spanning apertures of hundreds of meters, are insensitive to these effects and constrain the underlying fault.

We observe moderate profile-derived dips of ~60° at both ends of the Paso Superior fault, but much gentler dips of 0–30° along a ~2-km middle section (Figures 5a and 5b). Supplemental estimates from scarp trace-fitting exhibit a similar pattern, with mean dips and standard errors of 39° ± 2°, 11°, 15° ± 2°, and 37° ± 1°

in N-S order. The lowest dip angles can be confirmed visually from the raw displacement fields (Figure 3): this section of fault forms only a faint discontinuity in the vertical displacement field, reflecting small amounts of throw, but is much more prominent in the horizontal displacement fields, reflecting larger amounts of heave. The steeper dips along the outer segments are within the range of 50°–71° estimated from coarse-scale geodetic modeling in this area (Figure 1e), but the central structures have much shallower dips that agree within error with the ~20° dip of the Paso Superior fault recorded by Fletcher et al. (2014).

Within the Paso Inferior accommodation zone, we only inspect the longest (~4 km), W dipping strand. West and south of this strand, a set of shorter and highly distributed E dipping scarps, which are thought to belong to a 20–45° NE dipping detachment, may be the locally more important structure but they are too discontinuous to form part of our analysis. Measurements of the W dipping strand are hampered by noise, which is relatively large due to smaller slip values of 1–2 m compared to the other faults analyzed here (Figure 5c). Nevertheless, we observe systematic variations in both fault dip—with very shallow (up to subhorizontal) inclinations along the northernmost ~1 km of the fault, steepening abruptly to 60–90° along the southern ~3 km—and total slip, which increases from ~1 m to ~2 m concordantly. Our slip estimates always exceed those of Fletcher et al. (2014), implying that much of the deeper slip is lost to off-fault deformation in the near-surface. Additionally, where we calculate shallow dip angles of <30° (from ~0–1 km on Figure 5c), field dip measurements are consistently ~60°. This discrepancy might reflect steepening (refraction) of the fault toward the free surface, but we caution that the low signal to noise in offset measurements along this section (which sum to <1.2 m in total slip) might give rise to large errors in computed dip. The abrupt change in fault dip, if genuine, would imply that this fault strand is a relatively minor structure confined to shallow depths, consistent with its short length and subdued topographic signature.

Pronounced short-wavelength scatter in dip at the northern end of the Borrego fault (Figure 5d) most likely reflects that the rake here approaches 180°, indicating predominantly right-lateral slip (two of the measurements are above the cutoff of 160°). Nevertheless, dip measurements cluster between 60° and 80° along the northern half of the fault, and between 40° and 60° along the southern half, mimicking a trend in the field measurements. In contrast, satellite geodetic models approximate the Borrego fault as a single plane with a dip ranging from 50° to 75° (Figures 1d–1f). The Borrego fault is highly curvilinear, perhaps indicating linkages between diverse, shorter fault segments (Fletcher et al., 2014), and so we regard the southward reduction in dip angle captured in the field and lidar data as real. However, whereas field measurements of surface slip are extremely heterogeneous, our computed slip varies smoothly, increasing from ~1 m in the north to ~3 m in the south. Where our computed slip values disagree within error from field measurements (most notably from ~2.5–3.5 km on Figure 5d), the field measurements are the smaller of the two.

We resolve a continuous fault trend across the Puerta accommodation zone, although there are particularly bad striping artifacts in this area (Glennie et al., 2014) that make it challenging to determine accurate slip vectors (Figures 4a–4c). Consequently, our slip estimates display short-wavelength along-strike scatter in the order of ±1 m (Figure 4d). Estimates of dip are further hampered by a strongly right-lateral rake that often exceeds our 160° cutoff, as well as our gross simplification of the fault strike, which may vary considerably across this region of steep, mountainous topography. Consequently, we consider that only the *average* results for this section—a northeastward dip of ~60° and slip of ~2 m—are robust. There are no field estimates of fault dip to compare against, but our estimated dip of ~60° is consistent with values of 50–75° from coarse space geodetic models (Figures 1d–1f). The moderate dip angle, coupled with the local rugged topography, may explain why the surface trace of the displacement discontinuity appears undulating in map view (mostly clearly evident in Figure 4c).

Finally, computed dip angles along the Pescadores and Laguna Salada faults in the southernmost Sierra Cucapah are highly variable, reflecting the predominantly right-lateral sense of slip; in fact, all dip values along the southern half of this section are filtered from Figure 5e due to rake exceeding 160°. Nevertheless, along the northern Pescadores fault our average dip of ~70° is in agreement with field measurements (Fletcher et al., 2014), geodetic models (Figures 1d–1f), and estimates based on planar fitting of the fault trace using lidar topography (Zhou et al., 2016). However, our computed slip measurements differ from those of Fletcher et al. (2014). We observe an isolated peak of ~6 m on the central Pescadores fault where, locally, Fletcher et al. (2014) measure only ~2 m. We also consistently resolve larger values of slip than Fletcher et al., 2014's along the southern half of this fault and the neighboring Laguna Salada fault (ours average ~3 m, theirs ~2 m). This likely indicates a significant shallow slip deficit along these faults.

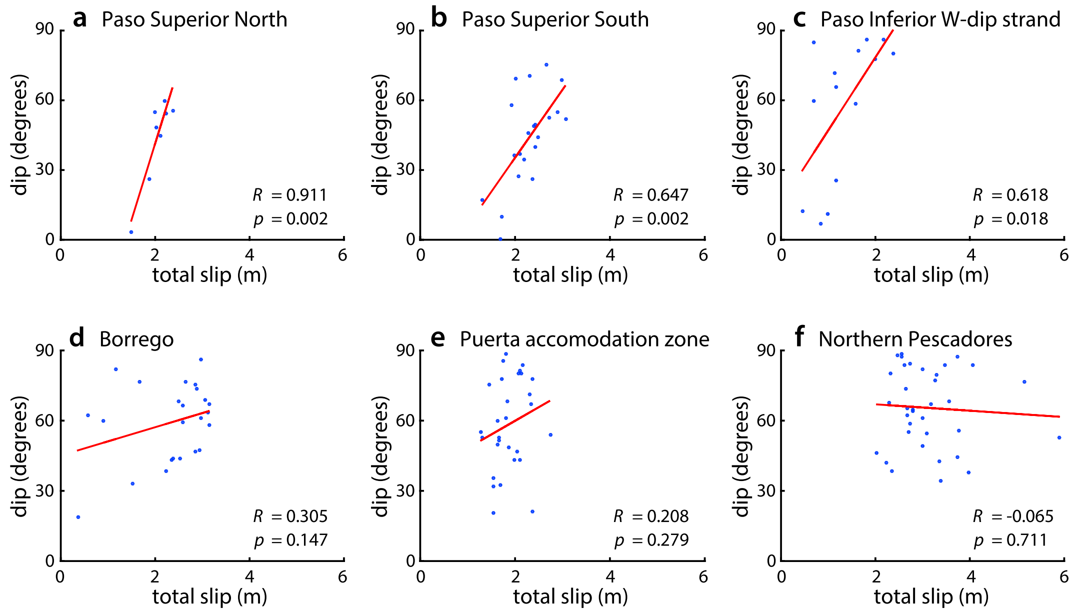

Figure 6. Slip and dip measurements (blue circles) with best fit linear trends (red lines) for (a, b) the Paso Superior fault, (c) the longest, W dipping strand of the Paso Inferior accommodation zone, (d) the Borrego fault, (e) the Puerta accomodation zone, and (f) the northern Pescadores fault. We do not include the southern Pescadores or Laguna Salada faults in this analysis because our dip calculation method fails (i.e., produces largely unconstrained results) for this stretch of fault due to rake values that approach pure strike slip (e.g., 0° or 180°/−180°). We therefore only plot results here for the northern section of the Pescadores fault: from 0 to 10.2 km in Figure 5e.

5. Discussion

Over a ~2-km section of the Paso Superior fault, our results confirm that the field-based observations and inferences of low-angle (<30°) oblique-normal coseismic slip (Fletcher et al., 2014) are not merely surficial phenomena but are also characteristic of the larger apertures sampled by the lidar. Because we do not observe any major inflections in the displacement field within the ~3-km-wide differential lidar swath, we contend that the low-angle slip must extend over a distance of at least 1–2 km from the fault surface trace, and therefore probably at least several hundred meters into the subsurface. We also observe gentle dip angles of ~30° along a shorter (~1 km) section of the W dipping Paso Inferior fault.

Throughout the central and northern Sierra Cucapah, satellite geodetic models of the earthquake yield much steeper dip estimates (50–75°) than lidar and field measurements along the same stretches of fault. These models also oversimplify the complex surface rupture in this area, by amalgamating several left-stepping, en echelon faults onto a continuous, nearly linear trace. This oversimplification, and the resulting modeling trade-offs with fault surface trace location and strike, may account for why these models fail to capture an important signal of shallow-angle slip (Fialko et al., 2010; Huang et al., 2017; Wei et al., 2011; Xu et al., 2016). Conversely, these coarse geodetic models—together with the various seismological solutions for the El Mayor-Cucapah earthquake (Figure 1c)—are likely to characterize best the deeper part of the fault zone, which is poorly sampled by the narrow differential lidar footprint. We note that aftershock locations and mechanisms also appear inconsistent with deep slip along a possible northeastward extension of the shallowly dipping Paso Superior fault beneath the Mexicali Valley (Hauksson et al., 2011). We therefore envisage that deep-seated slip along subvertical faulting transfers onto shallow, low-angle faulting in the northern Sierra Cucapah, perhaps because no more favorably oriented structure is available for reactivation in this area (though we have not confirmed this with structural observations in the field).

Figures 5a–5c reveals an apparent correlation between fault dip and slip magnitude along the Paso Superior and Paso Inferior faults. We test these relations statistically, calculating correlation coefficients (R) of 0.911 for the northern Paso Superior fault segment, 0.647 for the southern segment, and 0.618 for the Paso Inferior fault (Figures 6a–6c). Correlations for all three fault segments are maximized at zero lag. We use a p test to determine correlation significance—testing the null hypothesis that there is no relationship between observed phenomena. We find that we can reject the null hypothesis—and confirm statistical correlation between dip and slip magnitude—at the 95% confidence level. Similar analyses for the remaining faults yields R values of 0.305, 0.208, and −0.065 for the Borrego, Puerta, and northern Pescadores faults, respectively, with p tests indicating no correlation or weak correlation along these faults (Figures 6d–6f).

Overall, these results suggest that along the northernmost fault strands, fault dip is providing a first-order control on slip magnitude. For normal faults, with the maximum principal stress oriented vertically, Andersonian mechanics predicts optimally oriented fault dip angles of ∼60°; the less favorably oriented the fault is, the more difficult it is to slip (Anderson, 1905, 1951). The low-angle central Paso Superior fault appears to depress surface slip, whereas steeper sections of faulting to the north and south permit slip to break the surface relatively uninhibited. Similar relations hold for the Paso Inferior fault, with lidar-derived fault slip depressed according to the misalignment of the fault dip from the ideal Andersonian case. The northwestward decrease in dip angle along the Paso Inferior fault may have even prompted the northwestward propagating rupture to jump onto the neighboring, steeper southern Paso Superior fault (Figures 5b and 5c).

In summary, building upon earlier observations by Fletcher et al. (2014) and Teran et al. (2015), we demonstrate the importance of inherited structures in guiding the surface rupture trace of the El Mayor-Cucapah earthquake and controlling variations in shallow slip magnitude along it. This work adds to a growing number of studies that highlight the first-order role of geological fabric in governing the surface expression of large earthquakes, as well as the importance of high-resolution imagery and imaging geodesy in resolving this behavior (e.g., Avouac et al., 2006; Choi et al., 2018; Lee et al., 2002; Vallage et al., 2016; Yue et al., 2005).

6. Conclusions

Three-dimensional surface displacements from differential lidar provide a new means of characterizing shallow faulting in large earthquakes, bridging an observational gap between far-field deformation imaged by traditional satellite geodesy and surface slip measured in the field. We use differential lidar to map the slip vector distribution and shallow fault geometry along the northern half of the 2010 El Mayor-Cucapah earthquake rupture. We observe subsurface low-angle (<30°) oblique-normal slip along a ∼2 km section of the Paso Superior fault, consistent with local field measurements, as well as along a ∼1 km section of the neighboring Paso Inferior fault. Geodetic models that characterize the earthquake at the scale of the seismogenic layer indicate steep faulting throughout this region, and the low-angle faults are thus probably reactivated only within the upper few kilometers. Nevertheless, this earthquake is among the first well-documented examples of seismic slip along a continental low-angle normal fault during the instrumental period, and justifies the interpretation that these are relevant active tectonic structures in regions of continental extension. As such, these structures should be considered as possible seismic sources in regional seismic hazard analyses and Coulomb stress change calculations. We also observe that slip along the low-angle structures is depressed relative to adjacent, steeper sections of faulting, with a statistically significant correlation between displacement magnitude and fault dip. At one fault segment boundary, rupture appears to have jumped from a low-angle structure onto a steeper neighboring faults. This suggests that fault dip provided a first-order control both on the path of the surface rupture and on the amount of localized surface slip.

Acknowledgments
This research was funded primarily through a Pakiser fellowship from Colorado School of Mines to L. J. L. and a United States Geological Survey (USGS) grant G12AC20042 to E. N., who also acknowledges ongoing support from the Natural Sciences and Engineering Research Council of Canada (NSERC) through Discovery Grant 2017-04029, the Canada Foundation for Innovation (CFI), the British Columbia Knowledge Development Fund (BCKDF), and the Canada Research Chair program. In addition, initial work on this earthquake was supported by the National Science Foundation (NSF) through award EAR1148319, and earlier work on lidar differencing by NSF through EAR1461574 and by the Southern California Earthquake Center (SCEC) through award 14101. The authors thank the Instituto Nacional de Estadistica y Geografia (INEGI) for making the preevent lidar survey available, the NSF-supported National Center for Airborne Laser Mapping (NCALM, award EAR1339015) for the postearthquake survey, and the NSF-supported Open Topography facility (awards EAR1557484, EAR1557319, and EAR1557330) for publicly hosting both data sets (OpenTopography, 2010, 2013). All maps in this paper were plotted using the NSF-supported *Generic Mapping Tools* software (Wessel et al., 2013). We are grateful to Brandon Dugan, Yvette Kuiper, and Paul Sava for discussing this work and Tom Rockwell and Rob Zinke for thoughtful reviews.

References

Abers, G. A. (1991). Possible seismogenic shallow-dipping normal faults in the Woodlark-D'Entrecasteaux extensional province, Papua New Guinea. *Geology*, *19*, 1205–1208.

Anderson, E. M. (1905). The dynamics of faulting. *Transactions of the Edinburgh Geological Society*, *8*(3), 387–402. https://doi.org/10.1144/transed.8.3.387

Anderson, E. M. (1951). *The dynamics of faulting and dyke formation with applications to Britain*. New York: Hafner Pub. Co.

Avouac, J.-P., Ayoub, F., Leprince, S., Konca, O., & Helmberger, D. V. (2006). The 2005, M_w 7.6 Kashmir earthquake: Sub-pixel correlation of ASTER images and seismic waveforms analysis. *Earth and Planetary Science Letters*, *249*, 514–528.

Axen, G. J. (1999). Low-angle normal fault earthquakes and triggering. *Geophysical Research Letters*, *26*, 3693–3696.

Axen, G. J., Fletcher, J. M., Cowgill, E., Murphy, M., Kapp, P., MacMillan, I., et al. (1999). Range-front fault scarps of the Sierra El Mayor, Baja California: Formed above an active low-angle normal fault? *Geology*, *27*, 247–250.

Barišin, I., Hinojosa-Corona, A., & Parsons, B. (2015). Co-seismic vertical displacements from a single post-seismic lidar DEM: Example from the 2010 El Mayor-Cucapah earthquake. *Geophysical Journal International*, *202*(1), 328–346.

Barnard, F. L. (1969). Structural geology of the Sierra de Los Cucapas, northeastern Baja California, Mexico and Imperial County, California (Ph.D. thesis), University of Colorado Colorado, Boulder, Colorado.

Castro, R. R., Acosta, J. G., Wong, V. M., Perez-Vertti, A., Mendoza, A., & Inzunza, L. (2011). Location of aftershocks of the 4 April 2010 M_w 7.2 El Mayor-Cucapah earthquake of Baja California, Mexico. *Bulletin of the Seismological Society of America*, *101*(6), 3072–3080.

Choi, J.-H., Klinger, Y., Ferry, M., Ritz, J.-F., Kurtz, R., Rizza, M., et al. (2018). Geologic inheritance and earthquake rupture processes: The 1905 $M \geq 8$ Tsetserleg-Bulnay strike-slip earthquake sequence, Mongolia. *Journal of Geophysical Research: Solid Earth*, *123*, 1925–1953. https://doi.org/10.1002/2017JB013962

Fialko, Y., Gonzalez, A., Gonzalez-Garcia, J. J., Barbot, S., Leprince, S., Sandwell, D. T., & Agnew, D. C. (2010). *Static rupture model of the 2010 $M7.2$ El Mayor-Cucapah Earthquake from ALOS, ENVISAT, SPOT and GPS Data*, pp. B2125. Pasadena, CA: American Geophysical Union, Fall Meeting.

Fletcher, J. M., Oskin, M. E., & Teran, O. J. (2016). The role of a keystone fault in triggering the complex El Mayor-Cucapah earthquake rupture. *Nature Geoscience*, *9*(4), 303.

Fletcher, J. M., & Spelz, R. M. (2009). Patterns of Quaternary deformation and rupture propagation associated with an active low-angle normal fault, Laguna Salada, Mexico: Evidence of a rolling hinge? *Geosphere*, *5*, 385–407.

Fletcher, J. M., Teran, O. J., Rockwell, T. K., Oskin, M. E., Hudnut, K. W., Mueller, K. J., et al. (2014). Assembly of a large earthquake from a complex fault system: Surface rupture kinematics of the 4 April 2010 El Mayor–Cucapah (Mexico)M_w 7.2 earthquake. *Geosphere*, *10*(4), 797–827.

Glennie, C. L., Hinojosa-Corona, A., Nissen, E., Kusari, A., Oskin, M. E., Arrowsmith, J. R., & Borsa, A. (2014). Optimization of legacy lidar data sets for measuring near-field earthquake displacements. *Geophysical Research Letters*, *41*, 3494–3501. https://doi.org/10.1002/2014GL059919

Gold, P. O., Oskin, M. E., Elliott, A. J., Hinojosa-Corona, A., Taylor, M. H., Kreylos, O., & Cowgill, E. (2013). Coseismic slip variation assessed from terrestrial lidar scans of the El Mayor-Cucapah surface rupture. *Earth and Planetary Science Letters*, *366*, 151–162.

González-Ortega, A., Fialko, Y., Sandwell, D. T., Alejandro Nava-Pichardo, F., Fletcher, J., González-García, J. J., et al. (2014). El Mayor-Cucapah (M_w 7.2) earthquake: Early near-field postseismic deformation from InSAR and GPS observations. *Journal of Geophysical Research: Solid Earth*, *119*, 1482–1497. https://doi.org/10.1002/2013jb010193

González-Ortega, J. A., González-García, J. J., & Sandwell, D. T. (2018). Interseismic velocity field and seismic moment release in Northern Baja California, Mexico. *Seismological Research Letters*, *89*(2A), 526–533.

Hauksson, E., Stock, J., Hutton, K., Yang, W., Vidal-Villegas, J. A., & Kanamori, H. (2011). The 2010 M_w 7.2 El Mayor-Cucapah earthquake sequence, Baja California, Mexico and southernmost California, USA: Active seismotectonics along the Mexican Pacific margin. *Pure and Applied Geophysics*, *168*, 1255–1277.

Hough, S. E., & Elliot, A. J. (2004). Revisiting the 23 February 1892 Laguna Salada earthquake. *Bulletin of the Seismological Society of America*, *94*, 1571–1578. https://doi.org/10.1785/012003244

Huang, M. H., Fielding, E. J., Dickinson, H., Sun, J., Gonzalez-Ortega, A., Freed, A. M., & Bürgman, R. (2017). Fault geometry inversion and slip distribution of the 2010 M_w 7.2 El Mayor-Cucapah earthquake from geodetic data. *Journal of Geophysical Research: Solid Earth*, *122*, 607–621. https://doi.org/10.1002/2016JB012858

Jackson, J. A., & White, N. J. (1989). Normal faulting in the upper continental crust: Observations from regions of active extension. *Journal of Structural Geology*, *11*, 15–36.

Kroll, K. A., Cochran, E. S., Richards-Dinger, K. B., & Sumy, D. F. (2013). Aftershocks of the 2010 M_w 7.2 El Mayor-Cucapah earthquake reveal complex faulting in the Yuha Desert, California. *Journal of Geophysical Research: Solid Earth*, *118*, 6146–6164. https://doi.org/10.1002/2013JB010529

Kyriakopoulos, C., Oglesby, D. D., Funning, G. J., & Ryan, K. J. (2017). Dynamic rupture modeling of the M7.2 2010 El Mayor-Cucapah earthquake: Comparison with a geodetic model. *Journal of Geophysical Research: Solid Earth*, *122*, 10,263–10,279. https://doi.org/10.1002/2017JB014294

Lee, J. C., Chu, H. T., Angelier, J., Chan, Y. C., Hu, J. C., Lu, C. Y., & Rau, R. J. (2002). Geometry and structure of northern surface ruptures of the 1999 $M_w = 7.6$ Chi-chi, Taiwan earthquake: Influence from inherited fold belt structures. *Journal of Geophysical Research*, *24*(1), 173–192. https://doi.org/10.1016/S0191-8141(01)00056-6

Meng, X., & Peng, Z. (2014). Seismicity rate changes in the Salton Sea geothermal field and the San Jacinto fault zone after the 2010 M_w 7.2 El Mayor-Cucapah earthquake. *Geophysical Journal International*, *197*, 1750–1762.

Milliner, C. W. D., Dolan, J. F., Hollingsworth, J., Leprince, S., Ayoub, F., & Sammis, C. (2015). Quantifying near-field and off-fault deformation patterns of the 1992 $M_w 7.3$ Landers earthquake. *Geochemistry, Geophysics, Geosystems*, *16*, 1577–1598. https://doi.org/10.1002/2014GC005693

Mueller, K., Kier, G., Rockwell, T., & Jones, C. H. (2009). Quaternary rift flank uplift of the peninsular ranges in Baja and Southern California by removal of mantle lithosphere. *Tectonics*, *28*, TC5003. https://doi.org/10.1029/2007TC002227

Mueller, K. J., & Rockwell, T. K. (1995). Late quaternary activity of the Laguna Salada fault in Northern Baja California, Mexico. *Geological Society of America Bulletin*, *107*, 8–18.

Nagy, E. A., Stock, J. M., & 16, 251-16 (2000). Structural controls on the continent-ocean transition in the northern Gulf of California, *105*. https://doi.org/10.1029/1999JB900402

Nissen, E., Krishnan, A. K., Arrowsmith, J. R., & Saripalli, S. (2012). Three-dimensional surface displacements and rotations from differencing pre- and post-earthquake LiDAR point clouds. *Geophysical Research Letters*, *39*, L16301. https://doi.org/10.1029/2012GL052460

Nissen, E., Maruyama, T., Ramon Arrowsmith, J., Elliott, J. R., Krishnan, A. K., Oskin, M. E., & Saripalli, S. (2014). Coseismic fault zone deformation revealed with differential lidar: Examples from Japanese $M_w \sim 7$ intraplate earthquakes. *Earth and Planetary Science Letters*, *405*, 244–256.

OpenTopography (2010). El Mayor-Cucapah earthquake (4 April 2010 rupture LiDAR scan. https://doi.org/10.5069/G9TD9V7D

OpenTopography (2013). 2006 INEGI Sierra Cucupah empirically corrected lidar dataset. https://doi.org/10.5069/G9S180F8

Oskin, M. E., Arrowsmith, J. R., Corona, A. H., Elliott, A. J., Fletcher, J. M., Fielding, E. J., et al. (2012). Near-field deformation from the El Mayor-Cucapah earthquake revealed by differential LIDAR. *Science*, *335*, 702–705.

Proffett, J. M. (1977). Cenozoic geology of the Yerington district, Nevada, and implications for the nature and origin of basin and range faulting. *Geological Society of America Bulletin*, *88*, 247–266.

Rockwell, T. K., Fletcher, J. M., Teran, O. J., Hernandez, A. P., Mueller, K. J., Salisbury, J. B., et al. (2015). Reassessment of the 1892 Laguna Salada earthquake: Fault kinematics and rupture patterns. *Bulletin of the Seismological Society of America*, *105*(6), 2885–2893.

Ross, Z. E., Rollins, C., Cochran, E. S., Hauksson, E., Avouac, J.-P., & Ben-Zion, Y. (2017). Aftershocks driven by afterslip and fluid pressure sweeping through a fault-fracture mesh. *Geophysical Research Letters*, *44*, 8260–8267. https://doi.org/10.1002/2017GL074634

Rymer, M. J., Treiman, J. A., Kendrick, K. J., Lienkaemper, J. J., Weldon, R. J., Bilham, R., et al. (2011). Triggered surface slips in southern California associated with the 2010 El Mayor-Cucapah, Baja California, Mexico, earthquake. Reston, VA: US Geological Survey.

Scott, C. P., Arrowsmith, J. R., Nissen, E., Lajoie, L., Maruyama, T., & Chiba, T. (2018). The M7 2016 Kumamoto, Japan, earthquake: 3D deformation along the fault and within the damage zone constrained from differential lidar topography. *Journal of Geophysical Research: Solid Earth*, *123*, 6138–6155. https://doi.org/10.1029/2018JB015581

Styron, R. H., & Hetland, E. A. (2014). Estimated likelihood of observing a large earthquake on a continental low-angle normal fault and implications for low-angle normal fault activity. *Geophysical Research Letters*, *41*, 2342–2350. https://doi.org/10.1002/2014GL059335

Suárez-Vidal, F., Munguía-Orozco, L., González-Escobar, M., González-García, J., & Glowacka, E. (2007). Surface rupture of the Morelia fault near the Cerro Prieto geothermal field, Mexicali, Baja California, Mexico, during the M_w 5.4 earthquake of 24 May 2006. *Seismological Research Letters*, *78*(3), 394–399.

Teran, O., Fletcher, J. M., Oskin, M. E., Rockwell, T. K., Hudnut, K. W., Spelz, R. M., et al. (2015). Geologic and structural controls on rupture zone fabric: A field-based study of the 2010 M_w 7.2 El Mayor-Cucapah earthquake surface rupture. *Geosphere*, *11*(3), 899–920.

Uchide, T., Yao, H., & Shearer, P. M. (2013). Spatio-temporal distribution of fault slip and high-frequency radiation of the 2010 El Mayor-Cucapah, Mexico earthquake. *Journal of Geophysical Research: Solid Earth*, *118*, 1546–1555.

Vallage, A., Klinger, Y., Lacassin, R., Delorme, A., & Pierrot-Deseilligny, M. (2016). Geological structures control on earthquake ruptures: The M_w7.7, 2013, Balochistan earthquake, Pakistan. *Geophysical Research Letters*, *43*, 10,155–10,163. https://doi.org/10.1002/2016GL070418

Wei, S., Fielding, E., Leprince, S., Sladen, A., Avouac, J.-P., Helmberger, D., et al. (2011). Superficial simplicity of the 2010 El Mayor-Cucapah earthquake of Baja California in Mexico. *Nature Geoscience*, *4*, 615–618.

Wei, M., Liu, Y., Kaneko, Y., McGuire, J. J., & Bilham, R. (2015). Dynamic triggering of creep events in the Salton trough, Southern California by regional M 5.4 earthquakes constrained by geodetic observations and numerical simulations. *Earth and Planetary Science Letters*, *427*, 1–10.

Wernicke, B. (1995). Low-angle normal faults and seismicity: A review. *Journal of Geophysical Research*, *100*, 20,159–20,174.

Wessel, P., Smith, W. H. F., Scharroo, R., Luis, J., & Wobbe, F. (2013). Generic mapping tools: Improved version released. *Eos, Transactions American Geophysical Union*, *94*, 409–410.

Xu, X., Tong, X., Sandwell, D. T., Milliner, C. W. D., Dolan, J. F., Hollingsworth, J., et al. (2016). Refining the shallow slip deficit. *Geophysical Journal International*, *204*(3), 1867–1886.

Yue, L.-F., Suppe, J., & Hung, J.-H. (2005). Structural geology of a classic thrust belt earthquake: the 1999 Chi-Chi earthquake Taiwan ($M_w = 7.6$). *Journal of Structural Geology*, *27*, 2058–2083.

Zheng, Y., Li, J., Xie, Z., & Ritzwoller, M. H. (2012). 5 Hz GPS seismology of the El Mayor-Cucapah earthquake: Estimating the earthquake focal mechanism. *Geophysical Journal International*, *190*, 1723–1732.

Zhou, Y., Walker, R. T., Elliott, J. R., & Parsons, B. (2016). Mapping 3D fault geometry in earthquakes using high-resolution topography: Examples from the 2010 El Mayor-Cucapah (Mexico) and 2013 Balochistan (Pakistan) earthquakes. *Geophysical Research Letters*, *43*, 3134–3142. https://doi.org/10.1002/2016GL067899